PAPER

Multi-scale study of thermal stability of lithiated graphite†

Zonghai Chen,[*a] **Yan Qin,**[a] **Yang Ren,**[b] **Wenquan Lu,**[a] **Christopher Orendorff,**[c] **E. Peter Roth**[c] **and Khalil Amine**[*a]

Safety remains a major issue for the graphite anode used in lithium-ion batteries. The thermal stability of lithiated graphite was studied by atomic-scale characterization and cell tests. The results revealed that the thermal decomposition of the solid–electrolyte interface is the most easily triggered chemical reaction in lithium-ion cells and plays a critical role in determining the battery safety. It was also shown that natural graphite containing a small amount of 3R graphite had much better thermal stability than mesocarbon microbeads that had no detectable 3R graphite.

Introduction

It is evident that lithium-ion batteries with high power and energy density will be the key energy storage technology to power long-range plug-in hybrid electric vehicles (PHEVs), and eventually pure electric vehicles (EVs); the impetus behind the development of this technology is to save depleting fossil fuels and protect the environment.[1,2] In the past 20 years, the electrochemical performance of lithium-ion batteries has been improved significantly. In the early 1990s, the practical capacity of an 18650 lithium-ion cell (a standard size of 18 mm in diameter and 65 mm in length) was about 0.9 A h. Now, a lithium-ion cell with the same size can easily deliver a much higher practical capacity of 2.6 A h, and prototype cells are capable of more than 3.0 A h. These continuous improvements and others have made lithium-ion batteries most attractive for the transportation application.[2] Yet, safety issues remain a major technological barrier.[3] Battery manufacturers are now able to produce high-quality lithium-ion cells, with less than one reported safety incident for every one million lithium-ion cells produced. However, this failure rate on the cell level is still too high for PHEVs and EVs, since several hundred large format lithium-ion cells will be needed to power a vehicle, and their failure rate will be dramatically increased (by almost 1000 times) when assembled in a battery pack. Thus, there is a worldwide effort to investigate the failure mechanisms of lithium-ion batteries and to develop mitigation technologies to improve their safety characteristics.[3]

The failure of a lithium-ion cell can be triggered by multiple factors such as overheating, high rate operation, overcharge/overdischarge, internal/external short circuiting, and mechanical damage. An effective mitigation technology must be based on the true failure mechanism as determined from component-level studies, and must be verified at a cell level to demonstrate the compatibility with other cell components. There have been numerous investigations into the thermal stability of de-lithiated cathode materials, discussing the effects of electrolyte

aChemical Sciences and Engineering Division, Argonne National Laboratory, 9700 South Cass Avenue, Argonne, IL, 60439, USA. E-mail: Zonghai.chen@anl.gov; Tel: +1-630-252-6551; amine@anl.gov

bX-Ray Science Division, Argonne National Laboratory, 9700 South Cass Avenue, Argonne, IL, 60439, USA

cAdvanced Power Sources R&D Department, Sandia National Laboratory, Albuquerque, NM, 87185, USA

† Electronic supplementary information (ESI) available: Movies showing the evolution of XRD profile of lithiated MCMB during thermal ramping. See DOI: 10.1039/c1ee01786a

---

Broader context

Lithium-ion batteries are promising to power hybrid electric vehicles and plug-in electric vehicles to reduce the consumption of fossil fuels and to reduce the emission of greenhouse gas. However, the poor safety characteristics of lithium-ion batteries have been the major technological barrier for large scale applications. There has been substantial R&D effort to enhance the tolerance of lithium-ion batteries to various abuse conditions like overcharge, overdischarge, physical damage, and high temperature exposure. The multi-scale study of this work demonstrates that the thermal decomposition of the solid–electrolyte interface (SEI) is the weakest chemical reaction that can be easily triggered and can lead to thermal runaway. Atomic level characterization also reveals that the SEI layer on materials containing 3R graphite shows higher thermal stability than that on 2H graphite. The outcome of this work and the continuous research on this subject can generate critical knowledge for designing safer anode materials for large format lithium-ion batteries.

---

composition,[4,5] the ratio of transitional metal elements,[6–13] and surface modification.[14–16] However, there have been much fewer reports on the anode side because mesocarbon microbeads (MCMB) have been the dominant material, with far fewer candidate materials being investigated than for the cathode. Silicon-based alloys are currently being developed as a high capacity anode material for high energy applications, but are still at the pre-mature stage.[17–19] Hence, the safety issues of silicon-based materials have not received much attention from the research community, as reflected by the lack of literature reports.[20] To date, the safety-related research on the anode has mainly focused on electrolytes and electrolyte additives that improve the thermal stability of the lithiated graphite.[20–29] For instance, lithium bis(oxalato)borate (LiBOB) has been consistently reported to improve the thermal stability of lithiated graphite,[22] but the reaction of LiBOB-based electrolytes toward de-lithiated cathodes completely reversed its benefit at the cell level.[24] Moreover, the high interfacial impedance of lithium-ion cells using LiBOB-based electrolytes further limited the application of this electrolyte additive in high-performance lithium-ion batteries.[30] Alternatively, lithium difluoro(oxalato)borate (LiDFOB) can provide similar protection to lithiated graphite as LiBOB does with limited increase in the interfacial impedance.[21,30] Chen et al.[21] suggested that LiDFOB be limited as an electrolyte additive to minimize the possible side reaction between LiDFOB and the delithiated cathode. In this work, we employed various methods to investigate the correlation between the intrinsic properties of different graphitic anode materials and their thermal stability in cell tests.

Experimental

Materials investigated

Four types of graphitic materials were investigated in this work: MCMB, SMG-N-7b, SMG-N-20, and SMG-Ns-15f. The basic physical and chemical properties of these materials are listed in Table 1, and their scanning electron microscopy (SEM) images are shown in Fig. 1. The four materials were investigated as-received from the suppliers without any in-house modification. The MCMB served as a control for those materials containing natural graphite. The SMG-N-20 is bulk natural graphite, whose average particle size is 19.5 μm, and specific surface area is

Table 1 Physical properties of four types of graphite investigated

	MCMB-1028	SMG-N-7b	SMG-N-20	SMG-Ns-15f
Description	MCMB	Surface-modified natural graphite	Natural graphite	Surface-modified natural graphite
Diameter, D_{50}/μm	11.8	11.1	19.5	21.6
BET surface area/m^2 g^{-1}	2.01	5.0	5.1	0.7
Activation energy^a/ kJ mol^{-1}	53	88	92	78

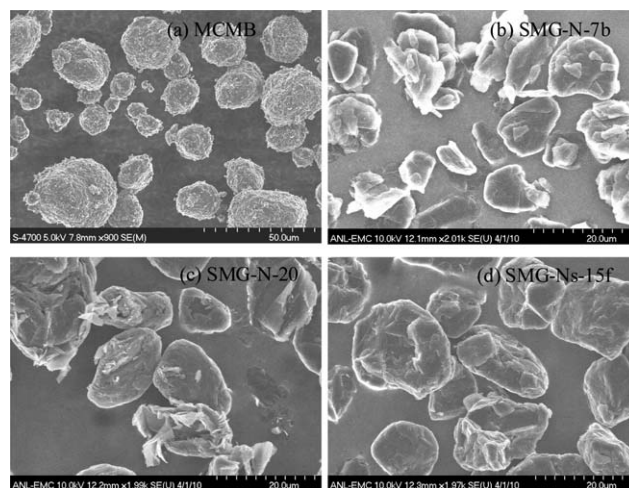^{a} Activation energy of decomposition for solid–electrolyte interface measured by Differential Scanning Calorimetry.

Fig. 1 SEM images of (a) MCMB, (b) SMG-N-7b, (c) SMG-N-20, and (d) SMG-Ns-15f.

5.1 m^2 g^{-1}. The SMG-Ns-15f has a similar particle size to SMG-N-20, but its surface was heavily coated with soft carbon to dramatically reduce its specific surface area to 0.7 m^2 g^{-1}. The SMG-N-7b has small particle size ($D_{50} = 11.1$ μm), similar to that of MCMB, with a light soft carbon coating to maintain a similar specific surface area (5.0 m^2 g^{-1}) to SMG-N-20.

Fabrication of 18650 cells

To investigate the effect of carbon materials on the safety of real lithium-ion cells, 18650 (standard size of 18 mm in diameter and 65 mm in length) lithium-ion cells were fabricated using the different graphite materials as the anode and LiFePO$_4$ as the cathode. The latter material was selected to minimize heat generation from the cathode and to emphasize the contribution from the anode. The electrolyte was 1.2 M LiPF$_6$ in a solvent mixture of ethylene carbonate (EC) and ethyl methyl carbonate (EMC) with a mass ratio of 3 : 7.

Scanning electron microscopy

A field-emission scanning electron microscope (Hitachi S-4700) at the Center of Electron Microscopy of Argonne National Laboratory was employed to observe the morphology and estimate the particle size of the graphite samples.

Accelerating Rate Calorimetry (ARC)

ARC testing was performed on 18650 cells (3.8 V LiFePO$_4$/graphite) at a 100% state of charge (SOC). The ARC (Arthur D. Little, Model 2000, AD Little, Acorn Park, Cambridge, MA) was operated in a heat–wait–search mode to allow determination of the onset of self-heating. The ARC increases the temperature in discrete steps, waits for the thermal transients to decay, and then monitors the temperature of the cell for a fixed time. If the cell temperature does not increase above a threshold value (typically 0.02 °C min^{-1}), the temperature is then increased by another step, and the process is repeated. If the cell temperature increases at a rate equal to or above the threshold value, the ARC switches to the exothermal mode, during which the ARC

temperature closely matches the cell temperature, thus maintaining an adiabatic state. The normal mode of operation of the ARC terminates an experiment by cooling the sample once it reaches a set upper temperature. The ARC experiment closely simulates a thermal abuse environment that includes moderately high temperatures for relatively long periods.

Differential Scanning Calorimetry (DSC)

The Li/graphite coin cells were first cycled between 1 mV and 1.5 V with a constant current of $C/10$ (0.25 mA) for two cycles before they were constant-voltage discharged to 1 mV. After the lithiation, the cells were then disassembled in the glovebox; the resulting red-brown electrodes were dried in the glovebox for 10 min before the preparation of samples for analysis by a Pyris 1 differential scanning calorimeter (DSC, Perkin Elmer). The major focus of this work was to investigate the impact of carbon material on the thermal stability of the solid–electrolyte interface (SEI). Therefore, to maintain the chemical integrity of the surface film, the harvested lithiated graphite samples were not rinsed. As a consequence, some residues, such as EC and LiPF$_6$, remained in the dried samples, adding uncertainty to the mass of the DSC samples. Since the fresh electrolyte comprising EC and LiPF$_6$ was further added to samples for DSC experiments, it is reasonable to assume that the residues did not add new reaction pathways to the thermal decomposition, and that the kinetics of the thermal reactions also remained unchanged. A typical DSC sample consisted of about 3.0 mg of solid material from the harvested electrode and about 3.0 μL of the electrolyte (1.2 M LiPF$_6$ in EC/EMC with a mass ratio of 3 : 7), and the sample was sealed in the Pyris 1 DSC cell. The heat flow detected was then normalized with the weight of the solid added. The relationship between the peak temperature and the scanning rate was used to determine the activation energy (E_a) of the SEI decomposition, as reported previously.[21]

In situ and *ex situ* high energy X-ray diffraction

The experimental setup for the *in situ* experiment was similar to that previously reported for solid-state synthesis.[31] A DSC sample contained in a stainless-steel high-pressure vessel was placed vertically in a programmable thermal stage, and the sample was heated up to 350 °C with a constant heating rate of 5 °C per minute. During the course of thermal ramping, a high-energy X-ray hits the sample horizontally, and a PerkinElmer area X-ray detector collects the X-ray diffraction (XRD) patterns in the transmission geometry with a speed of one spectrum per 20 seconds. The XRD experiment was carried out at the beamline 11-ID-C of the Advanced Photon Source (APS) of Argonne National Laboratory; the X-ray wavelength was 0.10987 Å. The collected 2D pattern was then integrated into conventional 1D data (intensity *vs.* 2θ) using the fit2d program.[32] The XRD patterns of the four graphitic anode materials were also collected at the same beamline by the same method, except at the ambient condition.

Raman spectroscopy

Raman spectra were acquired using a Raman microscope (Renishaw, inVia, at the Center of Nanoscale Materials of Argonne National Laboratory) with an excitation wavelength of 514 nm. All samples were measured using a 100× microscope objective to focus the laser excitation (10 mW) onto the samples as well as to collect the scattered light. The measurements were performed at room temperature.

Results

Raman spectroscopy

Fig. 2 shows the Raman spectra of the carbonaceous materials MCMB, SMG-N-20, SMG-Ns-15f, and SMG-N-7b. The strong and sharp peak at 1580 cm^{-1}, or so-called G band, represents the resonant absorption of ordered sp^2 carbon atoms in graphite. It can be seen that the G band of different graphite samples shows similar shape, intensity, and peak position. However, a big difference was observed for the D band at ~1350 cm^{-1} and D′ band at ~1620 cm^{-1}. Both D and D′ bands originate from the double resonance process of defective carbon atoms at disordered sites or edges of graphene sheets. Among the four materials investigated, MCMB shows the least signal from defective carbon atoms; it has the weakest D band intensity, and the D′ band is barely visible. Fig. 2 shows that the intensity of the D band and D′ band increases steadily in the order MCMB, SMG-N-20, SMG-N-7b, and SMG-Ns-15f. This order agrees well with the basic physical data presented in Table 1, as SMG-N-7b was slightly coated with soft carbon (mostly disordered), and SMG-Ns-15f was heavily coated with soft carbon to dramatically reduce its specific surface area.

X-Ray diffraction

While Raman spectroscopy provides surface-sensitive information to study local chemical bonding environments, XRD is a complementary technique to investigate the long-term ordering of atoms. Fig. 3 shows the XRD patterns of the four graphitic materials, and the diffraction peaks were successfully indexed using 2H and 3R graphite. Notice that the X-ray source was a high-energy X-ray beam (λ = 0.10987 Å) as opposed to the standard laboratory-scale copper K$_\alpha$ source (λ = 1.54 Å).
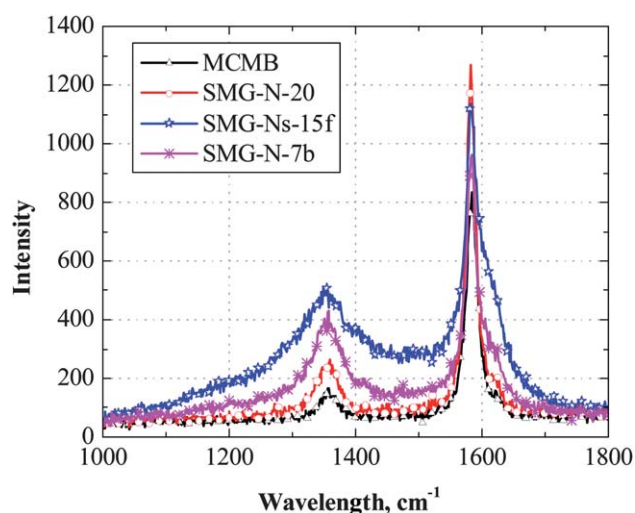

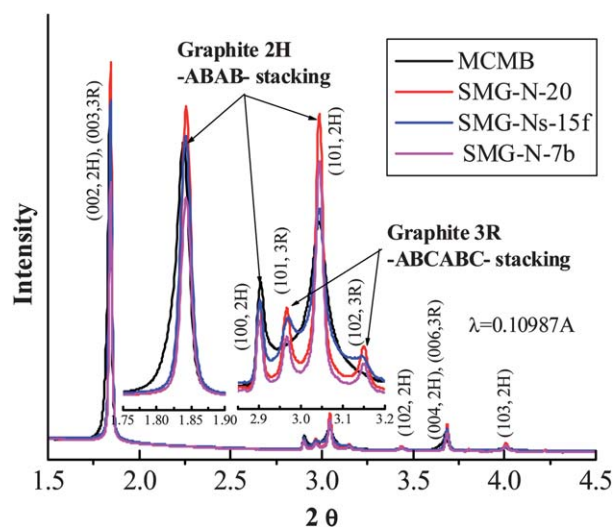**Fig. 2** Raman spectroscopy of four graphitic anode materials.

Fig. 3 XRD patterns of four graphitic anode materials using high-energy X-ray beam ($\lambda = 0.10978$ Å).

Therefore, the 2θ values in Fig. 3 are much smaller than those would be collected with a laboratory-scale X-ray diffractometer; but the XRD patterns remain comparable. All four samples showed a typical graphite structure, except that the MCMB curve had left shoulders on its (002) and (004) peaks. These left shoulders could have resulted from the special synthesis condition for MCMB at 2800 °C, at which graphite particles energetically prefer to form spherical beads to minimize the surface tension, and the formation of stacking defects (with bigger spacing between adjunct graphene sheets) is highly possible.

In contrast, the three natural graphite-based materials were synthesized at a much lower temperature, and because the natural stacking of graphene sheets was preserved, symmetrical diffraction peaks were observed. The inset of Fig. 3 in the 2θ range between 2.8° and 3.2° clearly shows that the XRD data have a high signal-to-noise ratio, with major differences among the four samples. The diffraction peaks at 2.91° and 3.04° are characteristic (100) and (101) peaks of 2H graphite, and the two at 2.96° and 3.14° are characteristic (101) and (102) peaks of 3R graphite.[33] The peaks indicate that 2H graphite is the major component of all four samples, and their content of 3R graphite varied. The inset of Fig. 3 also shows that MCMB has no or very low content of 3R graphite, SMG-Ns-15f has a low concentration of 3R graphite with poor long-term ordering (broadened diffraction peaks for 3R graphite), and SMG-N-20 and SMG-N-7b have high 3R graphite content.

The stacking difference between 2H and 3R graphite is schematically shown in Fig. 4. Both 2H and 3R graphite have an identical stacking block that is a graphene sheet, as shown in Fig. 4a. When stacking a second graphene sheet on the top of the base one, there are two equivalent ways of stacking: one is to shift the second sheet right by one C–C bond length, as indicated by the red solid arrow and the other is to shift the second sheet up and to the right by a C–C bond length, as illustrated by the green dashed arrow. The structure of 2H graphite can be considered as repeated stacking of the base graphene sheet (A, black one) and one of the offset graphene sheets (B, red one) in sequence, as shown in Fig. 4b and c. The 3R graphite can be visually
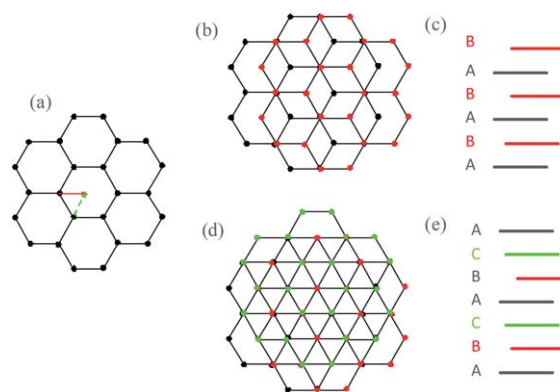

Fig. 4 Schematics of (a) graphene sheet as building blocks for graphite, (b) basal view of 2H graphite, (c) edge view of 2H graphite, (d) basal view of 3R graphite, and (e) edge view of 3R graphite.

reconstructed by repeating the base graphene sheet (A, black one), one offset graphene sheet (B, red one) and another offset graphene sheet (C, green one) alternately (see Fig. 4d and e).

Differential Scanning Calorimetry

We used DSC to investigate the effects of temperature up to 350 °C on various battery components. Current lithium-ion batteries are sensitive to temperature, and they can only work properly in a narrow temperature range. For instance, a fully charged lithium-ion cell will likely undergo thermal runaway when exposed to an external temperature of 140 °C or above.[24] This thermal runaway involves a set of self-accelerating chemical reactions, which, once triggered, can generate an exothermic heat flow that is larger than the heat dissipation rate to the environment. This excess heat increases the cell temperature, resulting in accelerated chemical reactions, exothermic heat flow, and higher temperature. Once triggered without external intervention, the thermal runaway will continue until the depletion of the reactants. Therefore, increasing the onset temperature of the self-accelerating reactions is the key to improving the thermal stability of lithium-ion batteries.[21]

Fig. 5 shows the DSC profile up to 350 °C for the following battery components: non-aqueous electrolyte (1.2 M LiPF$_6$ in EC/EMC with a mass ratio of 3 : 7), a mixture of delithiated cathode [Li$_{1-x}$(Li$_{0.1}$Mn$_{0.3}$Ni$_{0.3}$Co$_{0.3}$)O$_2$ at 4.1 V $vs.$ Li$^+$/Li] and a proper amount of nonaqueous electrolyte, a mixture of lithiated graphite (Li$_x$C$_6$ at 0.001 V $vs.$ Li$^+$/Li) and a proper amount of nonaqueous electrolyte, and a piece of Celgard 2325 separator. Two components, the separator and MCMB anode, had thermal events at a temperature below 200 °C. As shown in Fig. 5d, the separator exhibited endothermic reactions at 133 °C, 161 °C, and 165 °C, corresponding to melting the polyethylene and polypropylene components of the separator. The separator phase change alone (endothermic) does not directly contribute to heat generation and thermal runaway in lithium-ion cells. Fig. 5c shows a continuous exothermic plateau from 110 °C to ~230 °C at ~3 W g^{-1} for the lithiated MCMB combined with the nonaqueous electrolyte. We hypothesize that this plateau resulted from the continuous decomposition/formation of an SEI
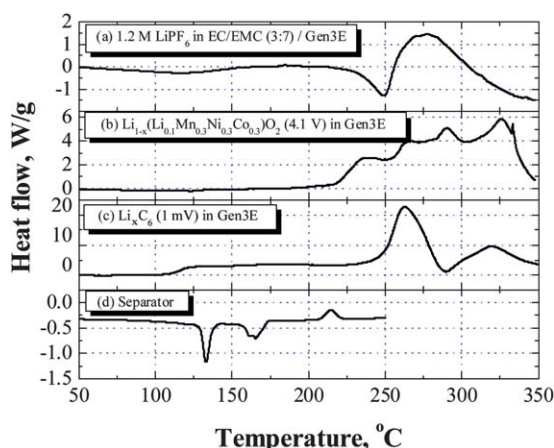
Fig. 5 DSC profiles of (a) 1.2 M LiPF$_6$ in EC/EMC (3 : 7 by weight) (Gen3E), (b) delithiated Li$_{1-x}$(Li$_{0.1}$Mn$_{0.3}$Ni$_{0.3}$Co$_{0.3}$)O$_2$ (at 4.1 V vs. Li$^+$/Li) with a proper amount of electrolyte (Gen3E), (c) lithiated MCMB Li$_x$C$_6$ (1 mV vs. Li$^+$/Li) with a proper amount of electrolyte (Gen3E), and (d) Celgard 2501 separator.

Fig. 6 Contour plot of *in situ* high-energy X-ray diffraction patterns of lithiated MCMB (Li$_x$C$_6$ at 1 mV vs. Li$^+$/Li) during thermal ramping and with the presence of nonaqueous electrolyte. The color of each pixel represents the detected X-ray intensity at specific 2θ values and specific temperatures. Red represents high intensity, and brown represents low intensity.

layer on the surface of the graphite anode,[34] leading to a constant, low-rate exothermic heat flow.

To validate this hypothesis, we performed an *in situ* high-energy X-ray diffraction (HEXRD) experiment to investigate the structural change of lithiated graphite during thermal ramping to 350 °C. Our sample consisted of 1.0 mg of lithiated graphite and 1.0 μL of nonaqueous electrolyte (1.2 M LiPF$_6$ in EC/EMC with a mass ratio of 3 : 7). This sample was prepared in our high-pressure stainless-steel DSC vessel. Because the high-energy X-ray beam ($\lambda = 0.10978$ Å) has excellent penetration capability, we were able to study the sample inside the stainless-steel vessel. Moreover, the high-flux X-ray source made it possible to collect XRD spectra with good signal-to-noise ratio at a rate of one spectrum for every 20 seconds.

Fig. 6 shows the contour plot of *in situ* HEXRD profiles during thermal ramping from 25 to 350 °C. The intensity of the XRD signal was color-coded, with red for high intensity and brown for low intensity. Initially, the (002) peaks for LiC$_6$ and LiC$_{12}$ were observed at 1.68° and 1.71° (2θ value), respectively. Due to the interference from a broad diffraction signal caused by the polyimide window on the thermal stage and the poly(vinylidene fluoride) (PVDF) binder in the sample, the weak diffraction peak of LiC$_{12}$ at 1.71° is difficult to observe in Fig. 6. Therefore, we include a movie as ESI† to show the evolution of the 1D XRD pattern for a clearer illustration. When the sample temperature was raised up to 110 °C, the diffraction peaks of LiC$_6$ and LiC$_{12}$ shifted to a lower angle due to the thermal expansion of the lattice without apparent change in the peak intensity. When the temperature was higher than 110 °C, the peak intensity of both LiC$_6$ and LiC$_{12}$ decreased steadily with temperature up to about 230 °C, above which the (002) peak of graphite was detected at 2$\theta = 1.82°$. We concluded that the content of lithium in the graphite decreased gradually during the thermal ramping from 110 to 230 °C. We believe this lost lithium was used for the continuous formation/decomposition of the SEI layer, as hypothesized previously.[34] Therefore, the SEI decomposition reaction is the main cause behind the self-accelerating reactions,
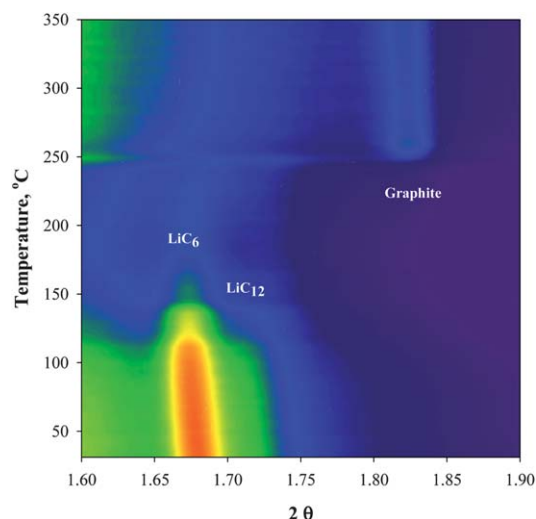
and the kinetics of SEI decomposition is the key to determining the thermal stability of lithiated graphite.

Fig. 7a shows DSC profiles of lithiated graphite in the presence of the nonaqueous electrolyte, 1.2 M LiPF$_6$ in EC/EMC (3 : 7 by weight). The common feature in the DCS curves of the four anode samples is that a slow exothermic reaction started at about 110 °C and continued until the major exothermic reaction at about 230 °C. Because the thermal decomposition of the SEI layer is the focus of this study, the DSC profiles in the range between 100 and 150 °C are shown as an inset in Fig. 7a. These profiles show that MCMB has a lower onset temperature and a higher level of exothermic heat flow than the natural-graphite-based materials, suggesting less stability for lithiated MCMB. Among the natural graphite samples, SMG-Ns-15f appears to be somewhat more reactive, but the differences are subtle. Therefore, identical anode samples were prepared, and DSC data were collected at different scanning rates to measure the peak temperature of SEI decomposition as a function of the scanning rate. We employed a model-independent equation[35] to determine the activation energy of the SEI decomposition reaction:

$$\ln\left(\phi/T_\mathrm{p}^2\right) = k - \frac{E_\mathrm{a}}{RT} \tag{1}$$

where ϕ is the scanning rate, T_p is the peak temperature, k is a constant, E_a is the activation energy, R is the ideal gas constant, and T is the absolute temperature. The relationship between ln (ϕ/T_p^2) and $1000/T$ is shown in Fig. 7b. The symbols show the experimental data, while the solid lines represent the fit to experimental data by using eqn (1); the activation energies are also listed in Table 1. The data show that SMG-N-20 had the highest activation energy (92 kJ mol^{-1}) and was therefore considered the most thermally stable. The thermal stability decreased in the order SMG-N-7b ($E_\mathrm{a} = 88$ kJ mol^{-1}), SMG-Ns-15f ($E_\mathrm{a} = 78$ kJ mol^{-1}), and MCMB ($E_\mathrm{a} = 53$ kJ mol^{-1}), in agreement with the DSC data in Fig. 7a.
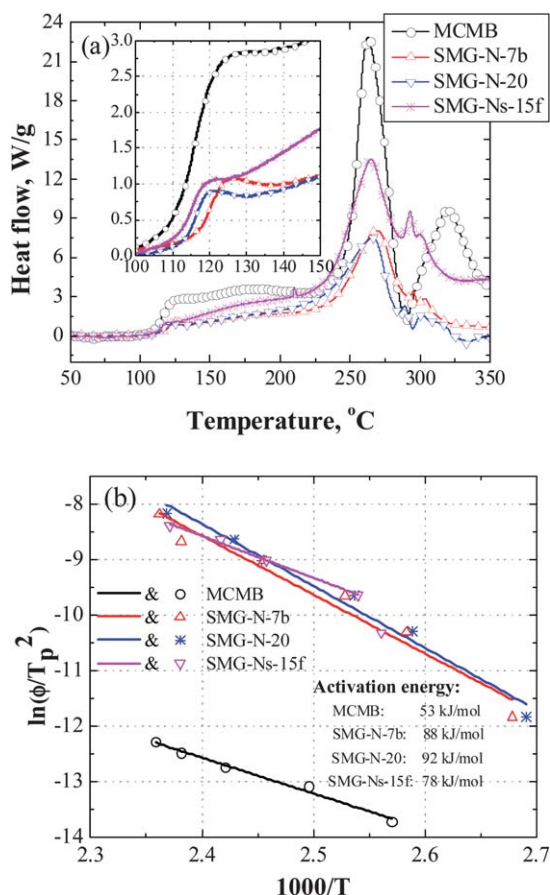
Fig. 7 (a) DSC profiles of lithiated graphite in the presence of a proper amount of nonaqueous electrolyte (1.2 M LiPF$_6$ in EC/EMC with a mass ratio of 3 : 7) and (b) plots of ln (ϕ/T_p^2) versus $1000/T$ to determine the activation energy of SEI decomposition.

Accelerating Rate Calorimetry of 18650 cells

To validate the kinetic results, we conducted ARC thermal abuse tests with 18650 lithium-ion cells (0.85 A h capacity) using a natural-graphite-based anode and LiFePO$_4$ cathode. The electrolyte for these cells was 1.2 M LiPF$_6$ in EC/EMC (3 : 7 by weight). Compared to other cathode materials based on transition metal oxides, delithiated Li$_{1-x}$FePO$_4$ is significantly more thermally stable and generates the least amount of heat during thermal abuse.[36] We chose LiFePO$_4$ for cell building to minimize the cathode contribution to the ARC measurement and to highlight the impact of graphite anodes. The initial ARC results to determine the effect of graphite materials on SEI stability were inconclusive. This was likely due to the variability in measuring the very low onset heating rates (0.02–0.1 °C min^{-1}) associated with SEI decomposition. Therefore, another set of 18650 cells was assembled with 2 wt% vinylidene carbonate (VC) as an electrolyte additive to form a thicker SEI layer.[37] We believed more SEI would give a greater onset response to thermal decomposition and more reproducibility among the tested cells.

Fig. 8 shows the ARC profiles of three 18650 cells using the natural-graphite-based anodes, LiFePO$_4$ cathode, and 2 wt% VC electrolyte additive. The onset temperature for the anode degradation of the SMG-Ns-15f cell is ~175 °C, while the SMG-

N-7b and SMG-N-20 cells show the onset at 185 °C. In addition, the peak heating rate for the SMG-Ns-15f cell is more than twice that of the other natural graphite cells, 0.7 vs. 0.3 °C min^{-1}. Note that the SMG-N-7b and SMG-N-20 cells have consistent ARC profiles in the anode decomposition regime (<220 °C). This finding suggests that the SMG-N-20 and SMG-N-7b cells have comparable reactivity during thermal runaway, and is consistent with the DSC and activation energy measurements on the anode materials. The SMG-Ns-15f cell is considerably more reactive and less thermally stable than the other two, which is also consistent with the DSC results.

Discussion

Thermal stability of SEI Layer and 18650 cells

The thermodynamic equivalent of the reaction between the lithiated graphite and the nonaqueous electrolyte can be broken down into two steps: (1) chemical deintercalation of lithium out of lithiated graphite, which is an endothermic process ($\Delta H > 0$), the energy for which is determined by the average working potential of the lithiated graphite; and (2) an exothermic reaction of lithium with nonaqueous electrolyte ($\Delta H < 0$). It is clear that the heat generated from the reaction between the lithiated graphite and the nonaqueous electrolyte is thermodynamically determined by the above two processes. The change of the SEI layer does not change the thermodynamics of the reaction (or the amount of heat generated), but does change the rate of heat generation and thereby improve the thermal stability of lithium-ion cells. This observation was supported by the agreement between the DSC and ARC results. The kinetics data obtained from DSC results showed that the activation energy of SEI decomposition for SMG-N-20 was slightly higher than that for SMG-N-7b and much higher than that for SMG-Ns-15f (see Fig. 7b). The ARC data showed that the cell using SMG-N-20 had similar thermal stability to that using SMG-N-7b, and was better than the cell using SMG-Ns-15f (see Fig. 8). This finding validated that the kinetics data at the component level (or DSC) are a reliable indicator to judge the thermal stability of the lithium-ion cell. Further research is needed on key factors that affect the thermal stability of the SEI layer.
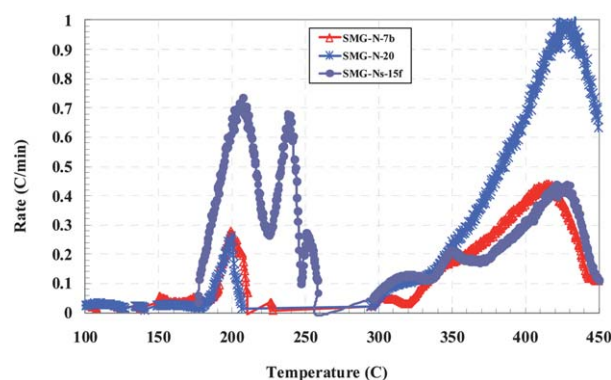

Fig. 8 ARC responses of 18650 cells using LiFePO$_4$ as the cathode, 2 wt% VC as the electrolyte additive, and SMG-N-20, SMG-N-7b, and SMG-Ns-15f as the anode.

4028 | *Energy Environ. Sci.*, 2011, **4**, 4023–4030

This journal is © The Royal Society of Chemistry 2011

Impact of surface area

It has been reported that a small specific surface area of active materials is highly desired for better safety performance of lithium-ion batteries.[38] The assumption is that if both the thickness and the chemical composition of the SEI layer are the same, an active material with larger specific surface area results in a larger amount of SEI material to be decomposed and greater exothermic heat flow. If this assumption is valid, then we can expect to see identical SEI decomposition kinetics for different samples. For the different anode materials in our study, the activation energy of the SEI decomposition varies greatly from sample to sample (see Table 1). The activation energy for SMG-N-20 with a specific surface area of about 5.1 m^2 g^{-1} is 92 kJ mol^{-1}, while the activation energy for MCMB (2.0 m^2 g^{-1}) is only 53 kJ mol^{-1}. In addition, SMG-N-20 has the highest specific surface area (5.1 m^2 g^{-1}) and SMG-Ns-15f has the smallest one (0.7 m^2 g^{-1}), but SMG-N-20 showed much better thermal stability than SMG-Ns-15f (see Table 1 and Fig. 8). For this particular case study, the specific surface area of graphite shows no direct correlation to the thermal stability.

Impact of soft carbon coating

Another possible variable in this set of graphite materials is the soft carbon coating. The D band signal at 1350 cm^{-1} from Raman spectroscopy shows good correlation to the expected content of the soft carbon coating (see Fig. 2). The SMG-Ns-15f was heavily coated with soft carbon while MCMB and SMG-N-20 showed very little disordered carbon. However, the kinetic data showed that the lithiated SMG-N-20 was the most thermally stable while the lithiated MCMB was the least (see Table 1). Therefore, no positive correlation between the soft carbon coating and the thermal stability could be established.

Impact of surface functional group

One variable that shows a positive correlation to the thermal stability of lithiated graphite is the presence of 3R graphite. The XRD patterns in Fig. 3 indicate that almost no 3R graphite was detected in MCMB. Fig. 3 also shows broadened and weak signature diffraction peaks of 3R graphite for SMG-Ns-15f and strong and well-defined peaks for both SMG-N-20 and SMG-N-7b. The same trend can also be seen for the thermal stability of lithiated graphitic anodes, as shown in Table 1 and Fig. 8. However, it is difficult to explain the kinetic results based upon the structural differences since both 2H graphite and 3R graphite have the same building block (graphene sheet) and identical spacing between adjunct graphene sheets. A possible explanation is the atomic level morphology at the edge of 2H graphite (Fig. 4c) is different from that of 3R graphite (Fig. 4e). This morphological difference might have a steric effect on the formation and decomposition of the SEI layer. Another possibility is that these anode materials were synthesized under different conditions, resulting in different surface functional groups at the graphite edge, which could affect the chemical composition of the SEI layer formed on this edge.[39,40] The characterization techniques used in our study here have limited capability to validate these two hypotheses, and strategic material synthesis is needed for that purpose.

Conclusion

Multi-scale characterization techniques were employed to investigate the safety characteristics of lithiated graphitic anodes. No positive correlation was established between the specific surface area, the presence of a soft carbon coating, or the thermal stability of lithiated graphite; however, the existence of 3R graphite correlated well with the thermal stability. It was proposed that either the local morphology at the edge of 3R graphite or the functional surface groups plays a key role in determining the kinetics of SEI decomposition.

Acknowledgements

Notes and references

1 T. H. Bradley and A. A. Frank, *Renewable Sustainable Energy Rev.*, 2009, **13**, 104–117.
2 H. Yang, S. Amiruddin, H. J. Bang, Y. K. Sun and J. Prakash, *J. Ind. Eng. Chem.*, 2006, **12**, 12–38.
3 T. M. Bandhauer, S. Garimella and T. F. Fuller, *J. Electrochem. Soc.*, 2011, **158**, R1–R25.
4 W. Y. Cui, M. Z. An, P. X. Yang and J. Q. Zhang, *Acta Physico-Chimica Sinica*, 2010, **27**, 78–84.
5 H. F. Xiang, H. Wang, C. H. Chen, X. W. Ge, S. Guo, J. H. Sun and W. Q. Hu, *J. Power Sources*, 2009, **191**, 575–581.
6 H. Bang, D. H. Kim, Y. C. Bae, J. Prakash and Y. K. Sun, *J. Electrochem. Soc.*, 2008, **155**, A952–A958.
7 W. B. Luo and J. R. Dahn, *J. Electrochem. Soc.*, 2010, **158**, A428–A433.
8 W. B. Luo, X. H. Li and J. R. Dahn, *J. Electrochem. Soc.*, 2010, **157**, A993–A1001.
9 W. B. Luo, X. H. Li and J. R. Dahn, *Chem. Mater.*, 2010, **22**, 5065–5073.
10 W. B. Luo, F. Zhou, X. M. Zhao, Z. H. Lu, X. H. Li and J. R. Dahn, *Chem. Mater.*, 2010, **22**, 1164–1172.
11 H. Y. Wang, A. D. Tang and K. L. Huang, *Chin. J. Chem.*, 2010, **29**, 27–32.
12 F. Zhou, W. B. Luo, X. M. Zhao and J. R. Dahn, *J. Electrochem. Soc.*, 2009, **156**, A917–A920.
13 F. Zhou, X. M. Zhao and J. R. Dahn, *J. Electrochem. Soc.*, 2010, **157**, A798–A801.
14 K. H. Choi, J. H. Jeon, H. K. Park and S. M. Lee, *J. Power Sources*, 2010, **195**, 8317–8321.
15 S. T. Myung, K. Amine and Y. K. Sun, *J. Mater. Chem.*, 2010, **20**, 7074–7095.
16 Y. K. Sun, D. H. Kim, C. S. Yoon, S. T. Myung, J. Prakash and K. Amine, *Adv. Funct. Mater.*, 2010, **20**, 485–491.
17 Z. H. Chen, V. Chevrier, L. Christensen and J. R. Dahn, *Electrochem. Solid-State Lett.*, 2004, **7**, A310–A314.
18 J. R. Szczech and S. Jin, *Energy Environ. Sci.*, 2011, **4**, 56–72.

19 W. J. Zhang, *J. Power Sources*, 2011, **196**, 13–24.
20 Y. D. Wang and J. R. Dahn, *J. Electrochem. Soc.*, 2006, **153**, A2188–A2191.
21 Z. H. Chen, Y. Qin, J. Liu and K. Amine, *Electrochem. Solid-State Lett.*, 2009, **12**, A69–A72.
22 J. Jiang and J. R. Dahn, *Electrochem. Solid-State Lett.*, 2003, **6**, A180–A182.
23 J. W. Jiang and J. R. Dahn, *Electrochim. Acta*, 2004, **49**, 4599–4604.
24 J. W. Jiang, H. Fortier, J. N. Reimers and J. R. Dahn, *J. Electrochem. Soc.*, 2004, **151**, A609–A613.
25 I. A. Profatilova, S. S. Kim and N. S. Choi, *Electrochim. Acta*, 2009, **54**, 4445–4450.
26 Y. Qin, Z. H. Chen, J. Liu and K. Amine, *Electrochem. Solid-State Lett.*, 2010, **13**, A11–A14.
27 Y. Qin, Z. H. Chen, W. Q. Lu and K. Amine, *J. Power Sources*, 2010, **195**, 6888–6892.
28 C. Taubert, M. Fleischhammer, M. Wohlfahrt-Mehrens, U. Wietelmann and T. Buhrmester, *J. Electrochem. Soc.*, 2010, **157**, A721–A728.
29 Q. S. Wang, J. H. Sun and C. H. Chen, *J. Hazard. Mater.*, 2009, **167**, 1209–1214.
30 J. Liu, Z. H. Chen, S. Busking and K. Amine, *Electrochem. Commun.*, 2007, **9**, 475–479.
31 Z. Chen, Y. Ren, Y. Qin, H. Wu, S. Ma, J. Ren, X. He, Y. K. Sun and K. Amine, *J. Mater. Chem.*, 2011, **21**, 5604–5609.
32 A. P. Hammersley, S. O. Svensson, M. Hanfland, A. N. Fitch and D. Hausermann, *Int. J. High Pressure Res.*, 1996, **14**, 235–248.
33 H. Lipson and A. R. Stokes, *Nature*, 1942, **149**, 328.
34 H. Yang, H. Bang, K. Amine and J. Prakash, *J. Electrochem. Soc.*, 2005, **152**, A73–A79.
35 H. E. Kissinger, *Anal. Chem.*, 1957, **29**, 1702–1706.
36 Y. G. Wang, P. He and H. S. Zhou, *Energy Environ. Sci.*, 2011, **4**, 805–817.
37 L. El Ouatani, R. Dedryvere, C. Siret, P. Biensan and D. Gonbeau, *J. Electrochem. Soc.*, 2009, **156**, A468–A477.
38 M. N. Richard and J. R. Dahn, *J. Electrochem. Soc.*, 1999, **146**, 2068–2077.
39 D. Bar-Tow, E. Peled and L. Burstein, *J. Electrochem. Soc.*, 1999, **146**, 824–832.
40 V. Eshkenazi, E. Peled, L. Burstein and D. Golodnitsky, *Solid State Ionics*, 2004, **170**, 83–91.